MATERIALS SCIENCE

Novel phase diagram behavior and materials design in heterostructural semiconductor alloys

Aaron M. Holder,[1,2]* Sebastian Siol,[1†] Paul F. Ndione,[1] Haowei Peng,[1‡] Ann M. Deml,[3] Bethany E. Matthews,[4] Laura T. Schelhas,[5] Michael F. Toney,[5,6] Roy G. Gordon,[7] William Tumas,[1] John D. Perkins,[1] David S. Ginley,[1] Brian P. Gorman,[3] Janet Tate,[4] Andriy Zakutayev,[1] Stephan Lany[1]*

Structure and composition control the behavior of materials. Isostructural alloying is historically an extremely successful approach for tuning materials properties, but it is often limited by binodal and spinodal decomposition, which correspond to the thermodynamic solubility limit and the stability against composition fluctuations, respectively. We show that heterostructural alloys can exhibit a markedly increased range of metastable alloy compositions between the binodal and spinodal lines, thereby opening up a vast phase space for novel homogeneous single-phase alloys. We distinguish two types of heterostructural alloys, that is, those between commensurate and incommensurate phases. Because of the structural transition around the critical composition, the properties change in a highly nonlinear or even discontinuous fashion, providing a mechanism for materials design that does not exist in conventional isostructural alloys. The novel phase diagram behavior follows from standard alloy models using mixing enthalpies from first-principles calculations. Thin-film deposition demonstrates the viability of the synthesis of these metastable single-phase domains and validates the computationally predicted phase separation mechanism above the upper temperature bound of the nonequilibrium single-phase region.

INTRODUCTION

The increasing demand for improved materials with precise and complex multiproperty functionality motivates moving beyond the traditionally explored area of near-equilibrium materials and calls for expanding the range of accessible phase space through the incorporation of metastability into materials design (*1*–*4*). Here, inspired by the great successes of alloying in isostructural systems to tailor materials for desired functionalities (*5*–*7*), we advance the application of materials design into metastable regimes. For heterostructural alloys (*8*), the transition between different crystal structures provides an additional degree of control for materials design beyond the effects of chemical substitution, and this additional control can affect a broad range of functionalities from optoelectronics (*3*, *4*, *8*) to piezoelectrics (*5*, *9*). These composition-induced phase transitions, encompassed under the evolving definition of morphotropic phase transitions (*10*), have received significant attention in the study of ferroelectric materials. However, the underlying heterostructural alloy physics is incompletely developed, and the composition-temperature phase diagrams have not been constructed or exploited for materials design. By incorporating the heterostructural alloy phase transformation into the construction of the phase diagram, we provide the thermodynamic criteria for evaluating the metastability and feasibility for predictive synthesis. The new phase diagram topologies that arise from heterostructural alloying have far-reaching implications for developing nonequilibrium materials that incorporate competing polymorph phases and phase segregation metastabilities into their design principles. Beyond the scope of inorganic semiconducting compounds studied here, this could include areas such as nanostructured alloys (*11*) and metallic glasses (*12*) used in industrial applications, nanoparticle dispersions (*13*, *14*) for pharmaceutical nanotechnologies, and the extensive set of applications enabled by homogeneous and bicontinuous phase polymers (*15*).

Isostructural alloy phase diagrams

$In_{1-x}Ga_xN$ is an example of a conventional isostructural alloy, well known for its role in enabling the solid-state lighting revolution (*16*–*18*), and Fig. 1 (A and B) shows the mixing enthalpy $\Delta H_m(x) = \Omega x(1 - x)$ and the resulting temperature (T) versus composition (x) phase diagram, respectively, within the regular solution model (*19*). From the free energy of mixing, $\Delta G_m(x,T) = \Delta H_m - T\Delta S_m$, one obtains the solubility limits for binodal and spinodal decomposition (*20*). Inside the spinodal region (gray in Fig. 1B), where ΔG_m has a negative curvature, the alloy decomposes spontaneously if kinetics allows sufficient atomic diffusion. At temperatures above the binodal line, the alloy is stable and thermodynamically fully miscible within a single phase. The binodal line $T^b(x)$ [Fig. 1B (blue)] describes the global free energy minimum and is found by the common tangent construction in $\Delta G(x,T)$. The spinodal line $T^s(x)$ (red) is determined by the condition $d^2/dx^2\Delta G_m(x,T) = 0$ and describes the stability of the alloy against composition fluctuations (*20*). Between the spinodal and binodal lines, the alloy is metastable; that is, free energy minimization tends to restore small composition fluctuations even when $\Delta G_m(x,T)$ lies above the phase-separated global free energy minimum. It is interesting to note that the same thermodynamic concepts apply also to liquid solutions, where one can observe the so-called "Ouzo effect" (*14*) when the system is brought into the metastable region by the addition of a third substance (that is, water). The resulting liquid-liquid dispersion with a

[1]National Renewable Energy Laboratory, Golden, CO 80401, USA. [2]Department of Chemical and Biological Engineering, University of Colorado, Boulder, CO 80309, USA. [3]Department of Metallurgical and Materials Engineering, Colorado School of Mines, Golden, CO 80401, USA. [4]Department of Physics, Oregon State University, Corvallis, OR 97331, USA. [5]Applied Energy Programs, SLAC National Accelerator Laboratory, Menlo Park, CA 94025, USA. [6]Stanford Synchrotron Radiation Lightsource, SLAC National Accelerator Laboratory, Menlo Park, CA 94025, USA. [7]Department of Chemistry and Chemical Biology, Harvard University, Cambridge, MA 02138, USA.
*Corresponding author. Email: aaron.holder@nrel.gov (A.M.H.); stephan.lany@nrel.gov (S.L.)
†Present address: Empa, Swiss Federal Laboratories for Materials Science and Technology, Überlandstrasse 129, 8600 Dübendorf, Switzerland.
‡Present address: Department of Physics, Temple University, Philadelphia, PA 19122, USA.

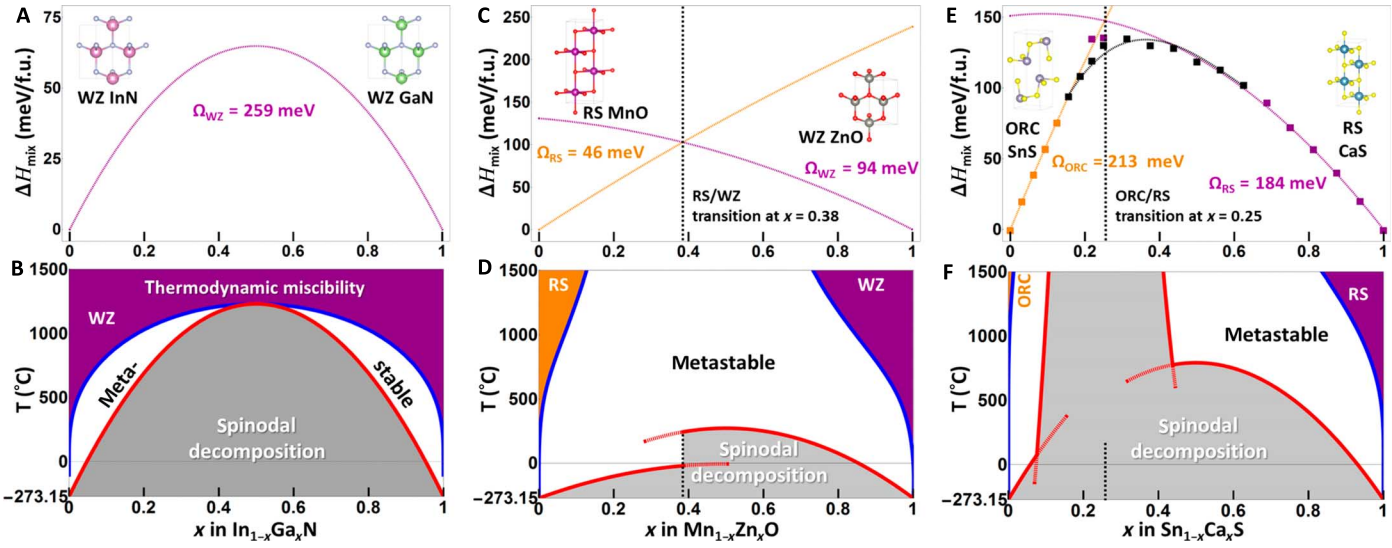

Fig. 1. Calculated mixing enthalpy $\Delta H_m(x)$ and resulting $T(x)$ phase diagram with binodal (blue) and spinodal (red) lines for three different cases of alloys. (**A** and **B**) Conventional case of an isostructural alloy, $In_{1-x}Ga_xN$, in the wurtzite (WZ) structure with the regular solution interaction parameter Ω = 0.26 eV from the study of Ho and Stringfellow (*19*). f.u., formula unit. (**C** and **D**) Heterostructural alloy formed from two materials with incommensurate lattices and $Mn_{1-x}Zn_xO$ formed from rock salt (RS) MnO and WZ ZnO. (**E** and **F**) Heterostructural alloy formed from materials with commensurate lattices and $Sn_{1-x}Ca_xS$ formed from orthorhombic (ORC) SnS and RS CaS. The spinodal gap is suppressed relative to the binodal gap in heterostructural alloys, producing a wider metastable region compared to the isostructural alloys.

milky appearance is a metastable phase with marked spatial uniformity, although the separation into hydrophilic and hydrophobic phases would have a lower free energy (*14*).

RESULTS

Heterostructural alloy phase diagrams

Here, we show that the phase diagrams of heterostructural alloys (Fig. 1, D and F) are markedly different from those of isostructural alloys, using $Mn_{1-x}Zn_xO$ (*3*) and $Sn_{1-x}Ca_xS$ (*4*) as example materials. These differences originate from the phase transition occurring in heterostructural alloys at a critical composition x_c. To elucidate the phase diagram behavior and demonstrate the realization of novel metastable alloys, we performed first-principles calculations and thin-film synthesis and characterization [mixing enthalpy and x-ray diffraction (XRD) data available from Peng *et al.* (*3*) are used for the $Mn_{1-x}Zn_xO$ alloys]. In the conventional isostructural $In_{1-x}Ga_xN$ alloy, the spinodal and binodal lines coincide at the miscibility gap temperature T^g and enclose relatively narrow regions of metastable compositions on either side of the phase diagram (white regions in Fig. 1B). We note that deviations from the regular solution model, arising as a result of short-range ordering, higher-order polynomial contributions in $H(x)$, and vibrational contributions to ΔH and ΔS, induce typically small quantitative changes and asymmetries in $T^{b,s}(x)$ but do not change the general topology (*21*). In contrast to the conventional isostructural phase diagram, our calculated heterostructural phase diagrams reveal wide metastable regions (Fig. 1, D and F) and the possibility of decoupling the miscibility gap temperatures for binodal and spinodal decomposition (Fig. 1D). This difference enables access to a novel phase space of metastable solid-state materials. The stability against composition fluctuations should facilitate the synthesis of homogeneous single-phase alloys, which are highly desirable for the design of optoelectronic materials.

As shown below, the nature of the phase transformation relating the different crystal symmetries of a heterostructural alloy has important ramifications on the topology of the alloy phase diagram. Therefore, we invoke the concepts of reconstructive and displacive phase transformations (*22*) to classify two different types of heterostructural alloys, exemplified by $Mn_{1-x}Zn_xO$ (Fig. 1, C and D) and $Sn_{1-x}Ca_xS$ (Fig. 1, E and F), respectively. Alloys between materials with incommensurate lattices, such as MnO with an RS ground state and ZnO with a wurtzite (WZ) ground state, have crystal symmetries that are related through a reconstructive transformation. This transition requires bond breaking, involves kinetic barriers, and is often associated with large changes in the lattice volume (for example, ~20% between RS and WZ). In contrast, alloys between materials with commensurate lattices, such as ORC SnS and RS CaS, have symmetries that are related by a displacive phase transformation. Here, structural distortions and atomic displacements lead to a continuous change of the lattice parameters and site positions without requiring atomic diffusion or rearrangement of the coordination environment.

In incommensurate lattices, combining the atomic arrangements of the two lattices within a single phase is energetically unfavorable, and sizable nucleation barriers impede the transformation between the phases. The $\Delta H_m(x)$ diagram of $Mn_{1-x}Zn_xO$ (Fig. 1C) shows the two separate mixing enthalpy branches for alloys formed on an underlying RS (orange) or WZ (purple) lattice, crossing and extending beyond the critical composition, which was calculated at x_c = 0.38 (*3*). Consequently, there are also two separate branches for the spinodal line (red) in the resulting $T^s(x)$ phase diagram (Fig. 1D), with a discontinuity at x_c. Because of the similar ionic size of Zn^{2+} and Mn^{2+}, the energetic contribution from the alloy interaction Ω to $\Delta H_m(x)$ in either branch is relatively small, such that the curvature of $\Delta H_m(x)$ is also small and its magnitude arises predominantly from the large polymorph energies of the end compounds (that is, the hypothetical RS ZnO and WZ MnO phases; cf. Fig. 1C). Consequently, the spinodal line decouples from the binodal line (Fig. 1D), in marked contrast to the well-known isostructural alloy phase diagram, where binodal and spinodal lines coincide at the miscibility gap temperature (Fig. 1B). Thus, as a result of the structural competition and ensuing transformation barriers in alloys with incommensurate

lattices, wide metastable regions emerge between the closed spinodal and the open binodal miscibility gaps. The only work we are aware of where both spinodal and binodal lines were constructed for heterostructural alloys is that of Schleife *et al.* (*8*). However, the enthalpy gain associated with the separation of the homogeneous single-phase alloy into two structurally different phases was not fully accounted for. Consequently, the phase diagram did not show the new features reported here and did not exhibit the experimentally established miscibility gap in $Mg_xZn_{1-x}O$ (*23*).

In the commensurate $Sn_{1-x}Ca_xS$ alloy at compositions near the ORC-RS phase transition at $x_c = 0.25$, we observe a lowering of the mixing enthalpy $\Delta H_m(x)$ compared to the extrapolation of the ORC (orange) and RS (purple) branches (Fig. 1E). The deviation from the extrapolated ORC and RS branches occurs because commensurate lattices can, to some extent, accommodate simultaneously the different preferred local coordination symmetries of both cation types. The increased curvature of $\Delta H_m(x)$ in this transition region leads to a "spike" of the spinodal line (red), resulting in a pseudoisostructural alloy character (cf. Fig. 1F), where the peaks of the binodal and spinodal lines coincide. At compositions outside of this transition region, however, the curvature is much smaller, again leading to wide metastable regions in the phase diagram.

Nonequilibrium phase diagrams and synthesizability

To experimentally test these remarkable new predicted features, we performed a nonequilibrium synthesis and characterization study of the two prototypical heterostructural semiconductor alloys. We used thin-film deposition techniques to overcome the solubility limits (binodal line) and access compositions and temperatures within the metastable areas in the phase diagrams. Libraries with gradients in composition and substrate temperature were grown by pulsed laser deposition (PLD) and sputtering for $Mn_{1-x}Zn_xO$ and $Sn_{1-x}Ca_xS$ alloys, respectively. As shown in Fig. 2A, the structural characterization by XRD as a function of composition illustrates the expected discontinuous change in structure occurring at the reconstructive phase transition in the incommensurate $Mn_{1-x}Zn_xO$ alloys. Conversely, we observe a much more continuous change in the structure of commensurate $Sn_{1-x}Ca_xS$ alloys (Fig. 2B).

We analyzed the alloy XRD patterns (Fig. 2, A and B) using the disappearing phase method (*24*) to determine the nonequilibrium single-phase growth regions. In $Mn_{1-x}Zn_xO$ alloys, we achieved complete miscibility over the full composition range $0 < x < 1$ for growth temperatures below 180°C (*3*). A fairly sharp transition from the RS into the WZ phase occurs at $x_c \approx 0.32$, slightly lower than the theoretically predicted value of $x_c = 0.38$. With increasing temperature, the solubility

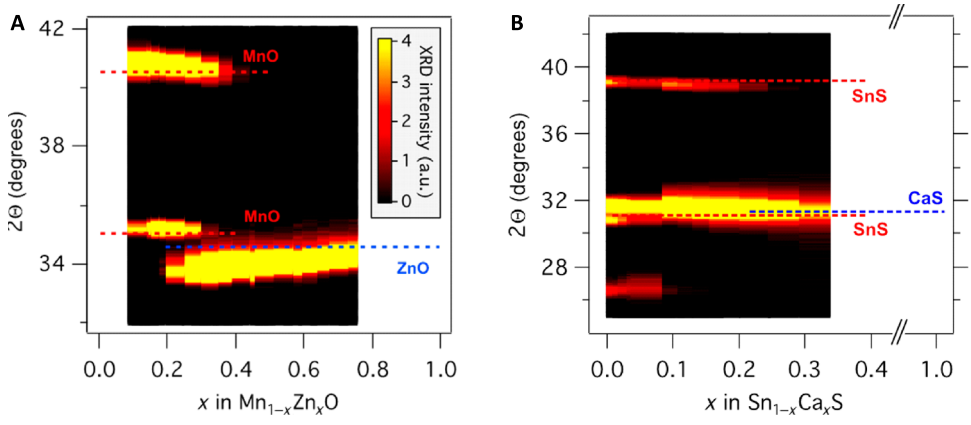

Fig. 2. Evolution of the structural properties of heterostructural alloys as a function of composition. XRD patterns of (**A**) incommensurate $Mn_{1-x}Zn_xO$ alloys exhibiting a discontinuous change of the structure with a two-phase region in the interval $0.2 < x < 0.4$ for the growth temperature of 297°C and (**B**) commensurate $Sn_{1-x}Ca_xS$ alloys grown at 240°C, showing a continuous change in the structure. a.u., arbitrary units.

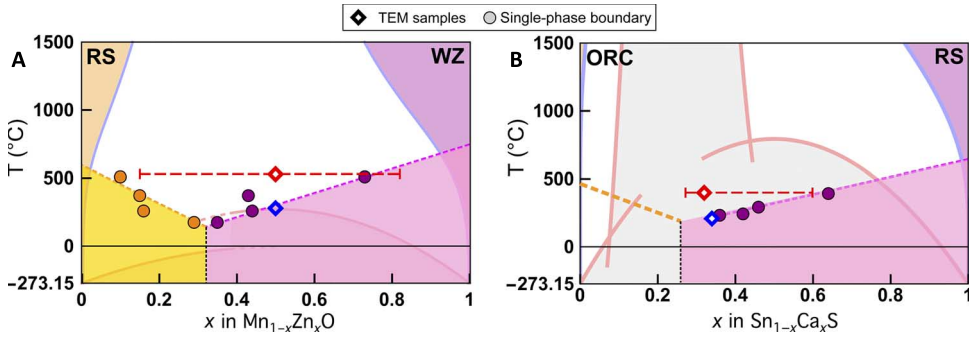

Fig. 3. Experimentally determined nonequilibrium phase diagrams. XRD derived nonequilibrium phase diagram of (**A**) $Mn_{1-x}Zn_xO$ and (**B**) $Sn_{1-x}Ca_xS$ overlaid on their respective calculated thermodynamic phase diagram (cf. Fig. 1). The circles show the single-phase boundary points obtained from the disappearing phase analysis of the XRD data and were used to determine the single-phase regions (shaded areas beneath dashed lines). For $Sn_{1-x}Ca_xS$ in the Sn-rich range $x < 0.25$, the single-phase boundary is estimated (see the main text). The diamonds indicate (x,T) combinations of samples grown to test the decomposition mechanism (see below), and the bars shown at the higher temperature indicate the composition variation, as determined by scanning transmission electron microscopy (STEM) with energy dispersive spectroscopy (EDS).

limits are reduced because the kinetics now allow for phase separation, thereby opening a miscibility gap with temperature against the thermodynamic trend. This result can be viewed as a manifestation of the Bell-Evans-Polanyi principle of kinetics (*25*, *26*) in a solid-state system; that is, the kinetic barriers to decomposition are the lowest where $\Delta H_m(x)$ is the largest, thereby explaining why the minimum temperature for nonequilibrium solubility occurs at x_c (cf. Figs. 1C and 3A). Applying the disappearing phase method to the diffraction patterns of the $Sn_{1-x}Ca_xS$ alloys grown by sputtering (Fig. 2B), we are able to determine the Sn nonequilibrium solubility limits in Ca-rich alloys (Fig. 3B). However, because of the commensurate structures of SnS and CaS, the changes in XRD are not prominent enough to unambiguously determine the Ca solubility limit in Sn-rich alloys from the experimental data. Applying the Bell-Evans-Polanyi–type behavior from the predicted $\Delta H_m(x)$ allows us to qualitatively estimate the nonequilibrium Ca solubility limit in ORC phase Sn-rich films (Fig. 3B).

DISCUSSION

Metastability and phase separation

An interesting difference arises between the nonequilibrium behaviors of the two alloy systems. The upper temperature boundary of the nonequilibrium single-phase region of $Mn_{1-x}Zn_xO$ lies above the predicted spinodal line. In contrast, in the case of $Sn_{1-x}Ca_xS$, most realizable compositions lie inside the spinodal gap, except for very large Ca (and perhaps Sn) fractions. This difference allows us to test the predicted alloy model by examining the decomposition process after growing films deliberately at temperatures above the single-phase boundary. Specifically, in the case of $Mn_{1-x}Zn_xO$, we expect a phase separation into RS MnO and WZ ZnO (binodal decomposition to the nonequilibrium solubility limits), whereas in $Sn_{1-x}Ca_xS$, we expect a spinodal decomposition process (nanoscale compositional fluctuations). To test these expectations, we grew two sets of single-composition films at temperatures inside and above the single-phase region (cf. Fig. 3, diamonds), that is, $Mn_{0.5}Zn_{0.5}O$ films at 300° and 550°C, as well as $Sn_{0.66}Ca_{0.34}S$ and $Sn_{0.68}Ca_{0.32}S$ films at 240° and 400°C, respectively. Subsequently, we characterized the samples by STEM-EDS. For the lower growth temperatures, the STEM-EDS analysis confirms that we have realized homogeneous single-phase films (Fig. 4, A and C). At the higher temperature (Fig. 4B), $Mn_{1-x}Zn_xO$ decomposes into a Mn-rich RS and into a Zn-rich WZ phase, in agreement with the predicted binodal decomposition process. The minimum and maximum of the composition variation determined by STEM-EDS agree well with the nonequilibrium solubility limits determined by XRD (cf. Fig. 3A). In contrast to $Mn_{1-x}Zn_xO$, the commensurate $Sn_{1-x}Ca_xS$ alloy system shows nanoscale composition modulations of Sn-rich and Ca-rich regions when grown at the higher temperature (Fig. 4D), signifying the predicted spinodal decomposition mechanism and further confirming the novel phase diagram features exhibited by heterostructural alloys. The growth of homogeneous $Sn_{1-x}Ca_xS$ films at the lower temperature within the spinodal gap is particularly remarkable because it demonstrates the kinetic inhibition of composition fluctuations, which is not required in the case of $Mn_{1-x}Zn_xO$. The kinetic control over compositional intertwining can also be used to develop new nanostructured materials with tunable heterogeneity and topological modification of properties.

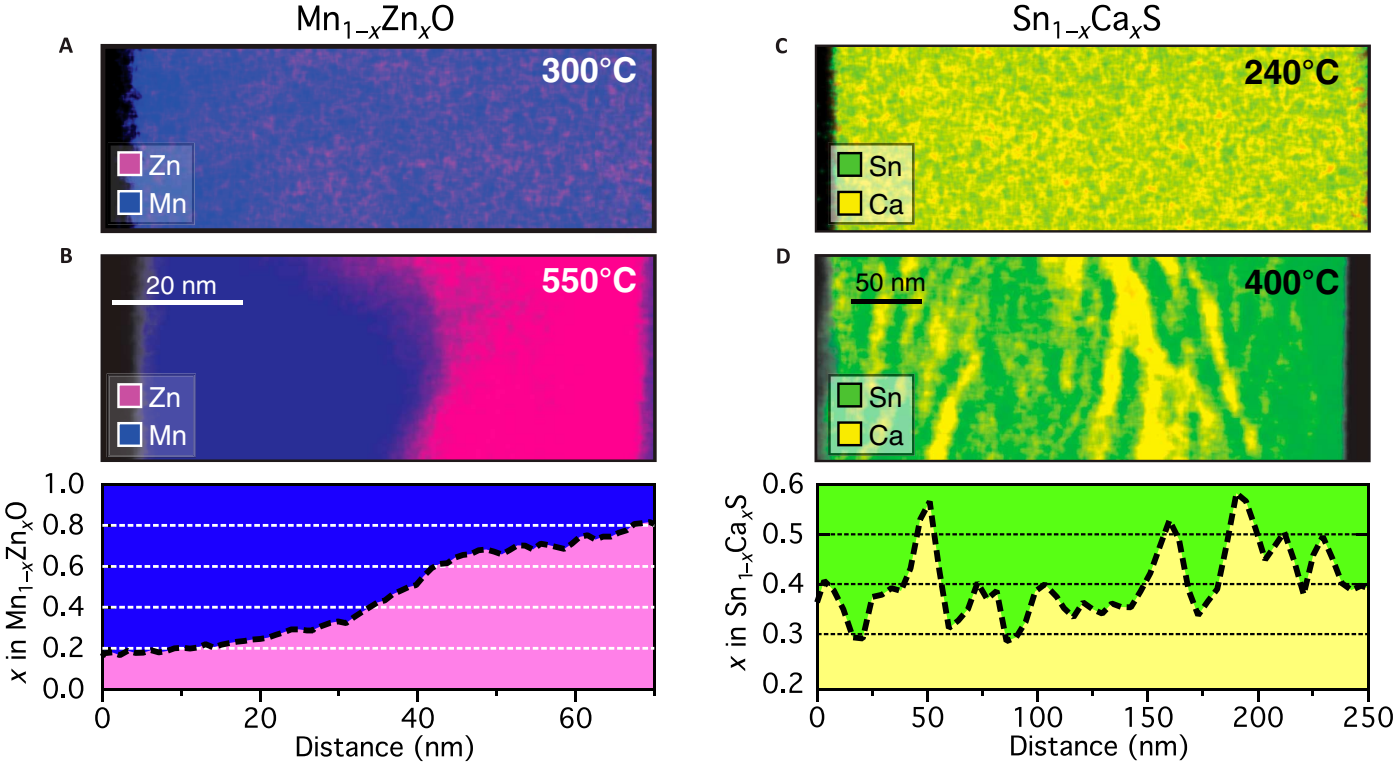

Fig. 4. Cross-sectional STEM-EDS spectral images of the heterostructural alloys grown at different substrate temperatures. (**A** and **C**) A homogeneous single-phase film is confirmed for the lower growth temperatures. At the higher temperature outside the single-phase region (cf. Fig. 3), a (binodal) phase separation is observed for $Mn_{0.5}Zn_{0.5}O$ (**B**), but a spinodal decomposition is observed for $Sn_{0.68}Ca_{0.32}S$ (**D**). One-dimensional linescan compositional profiles extracted from the two-dimensional (2D) spectral images are shown in the bottom panels, from which the quantified data in Fig. 3 were determined.

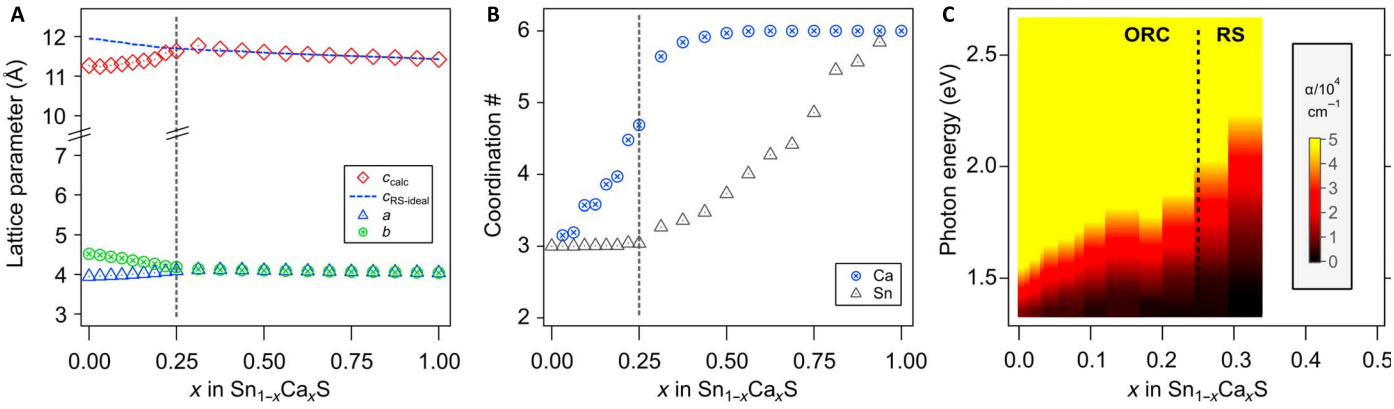

Fig. 5. Evolution of the structural parameters and optical absorption spectra of $Sn_{1-x}Ca_xS$ alloys as a function of the composition. The calculated lattice parameters (**A**) and cation coordination numbers (**B**) illustrate the continuous evolution of global and local lattice symmetries associated with the displacive-type phase transformation in commensurate heterostructural alloys. Note that the ORC structure of SnS can be derived from a $\sqrt{2} \times \sqrt{2} \times 2$ supercell of the conventional RS cell. Hence, the ideal $c/\sqrt{(a \cdot b)}$ ratio is $2\sqrt{2}$, and the c lattice parameter corresponding to this ideal ratio ($c_{RS\text{-ideal}}$) is shown by the blue dashed line in (A). The commensurate alloys therefore show a gradual change in the (**C**) optical properties due to the continuous evolution of the lattice symmetry. This example demonstrates the coupled utilization of composition-structure and structure-property relationships for materials design in heterostructural alloys.

It should be pointed out that the phase diagram behavior of heterostructural alloys follows from the energetics of the bulk materials and does not rely on any thin film–specific effects, such as substrate, strain, or stress. For the film thicknesses on the order of hundreds of nanometers used in our work, the immediate effects of substrate and dimensional confinement play a minor role. Therefore, similar phases should, in principle, exist in the bulk form. However, overcoming the binodal solubility limits to access the metastable regions of interest is prominently facilitated by using nonequilibrium thin-film synthesis routes.

Ramifications of heterostructural alloying on materials design

Finally, we wish to highlight the potential of heterostructural alloying for enabling new functionalities and for materials design in general. For example, in $Mn_{1-x}Zn_xO$ alloys, the change of the global symmetry (RS→WZ) enables beneficial band transport for holes while also reducing the band gap from the ultraviolet (UV; 3.5 eV) into the visible (Vis; 2.3 eV) region. These changes occurred at the critical composition in a discontinuous fashion and were instrumental in the demonstration of initial photoelectrochemical solar water splitting applications of these $Mn_{1-x}Zn_xO$ alloys (*3*). In the $Sn_{1-x}Ca_xS$ alloys, the change of the local coordination environment and global symmetry (ORC→RS), as shown by the computationally predicted compositional evolution of the lattice parameters and cation coordinations of Fig. 5 (A and B, respectively), should enable the control of the transport properties from the anisotropic transport in SnS (*27*) toward an isotropic transport above $x > 0.25$. At the same time, the optical absorption onset increases (Fig. 5C) and is expected to become more direct in character (*4*), suggesting this system for materials design in photovoltaic solar energy conversion applications. Alternatively, the substitution of isovalent elements with a different preferred coordination environment (for example, Ca for Sn) can also serve to reduce the thermal conductivity of the material, which is desirable for thermoelectric applications (*28*). Thus, the exploitation of the composition-structure and structure-property relationships in heterostructural alloying, as demonstrated here by the examples of $Mn_{1-x}Zn_xO$ and $Sn_{1-x}Ca_xS$, motivates the widespread adoption of this materials design strategy.

The alloy interaction parameter Ω, which determines the spinodal miscibility gap, depends largely on the ionic size mismatch between the alloy substituents (*20*). In contrast, the binodal gap depends on both the interaction parameter and the polymorph energy difference of the end-member compounds. Therefore, interesting novel metastable alloys may be more likely found in systems where the size mismatch is small but the polymorph energies are large enough to prevent the formation of a solid solution already under thermodynamic equilibrium conditions.

In conclusion, we have described a novel phase diagram behavior in heterostructural alloys, exhibiting markedly wide metastable regions with compositions beyond the thermodynamic solubility limit, which nevertheless are stable against spinodal decomposition. By controlling the growth kinetics in thin-film synthesis, we realized homogeneous single-phase $Mn_{1-x}Zn_xO$ and $Sn_{1-x}Ca_xS$ alloys deep inside the miscibility gap. Heterostructural alloying allows the exploration of a vast nonequilibrium phase space for materials by design, using structure-property and composition-structure relationships simultaneously. This novel design principle will facilitate the development of new materials with uniquely tailored properties and desired functionalities.

MATERIALS AND METHODS

First-principles calculations

All atomic structure and total energy calculations were performed within the Vienna Ab Initio Simulation Package (*29*), using the projector augmented-wave method (*30*). For density functional theory (DFT), we used the Perdew-Burke-Ernzerhof (PBE) generalized gradient approximation exchange-correlation functional (*31*). To obtain very accurate polymorph energies, which are important for realistic mixing enthalpies (cf. Fig. 1, A, C, and E), we performed total energy calculations for MnO and ZnO in the random phase approximation in a previous study (*32*) based on the adiabatic-connection fluctuation-dissipation theorem (RPA-ACFDT) (*33*). For the present work, we performed RPA-ACFDT calculations for SnS in the ORC and RS structures with specifications as given in our previous study (*32*). For incommensurate alloys, the DFT mixing enthalpy can be corrected using the RPA polymorph energies (*3*), whereas in commensurate alloys, $\Delta H_m(x)$ must be

evaluated with an energy-corrected functional. For this purpose, we used a PBE + $V_{Sn\text{-}p}$ approach, where the onsite potential (*34*) $V_{Sn\text{-}p}$ = −0.5 eV acts on the Sn-*p* states to increase the hybridization with the occupied orbitals, thereby increasing the stereoactivity and resulting in $E_{RS} - E_{ORC}$ = 153 meV, in agreement with the RPA energy difference. The mixing enthalpies were then determined using 256-atom supercells with random cation configurations. $\Delta H_m(x)$ was fitted with a second-order polynomial separately for all branches shown in Fig. 1 (A, C, and E), expect for the transition region in $Sn_{1-x}Ca_xS$ for which a third-order polynomial was used. With the configurational entropy of the random alloy $\Delta S = -k_B[x\ln x + (1-x)\ln(1-x)]$, the phase diagram was obtained from ΔG_m by constructing the lowest-energy common tangent across all branches and evaluating the zero-curvature condition for the individual branches separately.

Combinatorial growth and characterization

For an accelerated screening of the composition-temperature deposition phase space, a high-throughput approach was used, which includes combinatorial synthesis (*35*), spatially resolved characterization, and semiautomated data analysis (*36*). By applying intentional and well-controlled orthogonal gradients of composition and temperature (*37*) on the 2-inch × 2-inch SiO_2 substrate, several values of these deposition parameters were covered in a single synthesis experiment. The (Sn,Ca)S composition spread was achieved via RF cosputtering from 2-inch ceramic SnS and CaS targets. The $Mn_{1-x}Zn_xO$ libraries were grown using PLD from MnO and ZnO targets, as previously described by Peng *et al.* (*3*). In both alloy cases, several libraries were deposited using different sputter powers and pulse counts to produce thin films over the entire alloy composition range. The resulting sample libraries were analyzed at 44 points (4 × 11 grid) via automated, spatially resolved techniques, with respect to their composition [x-ray fluorescence (XRF)], crystal structure (XRD), film thicknesses (ellipsometry or XRF), and optoelectronic properties (UV-Vis spectroscopy and four-point probe). Focused ion beam and scanning electron microscopy were used to site-specifically prepare and extract specimens of particular composition and temperature from the sample libraries. Further analysis by transmission electron microscopy (TEM) allowed for nanoscale quantification of the material composition, crystallographic structure, and any spatially varying microstructural features. A detailed description of the experimental methods follows.

Combinatorial growth

The depositions of the $Sn_{1-x}Ca_xS$ libraries were carried out through RF magnetron sputtering in a custom UHV sputter tool (AJA International) with a base pressure of 2×10^{-7} mbar. Thin $Sn_{1-x}Ca_xS$ libraries were deposited on 2-inch × 2-inch fused silica substrates with a thickness of 1.5 mm. The substrates were heated through a partial thermal contact with a heated sample holder. This setup resulted in a temperature gradient across the library ranging from 400°C on the hottest side to 240°C on the coldest side. A more detailed description of this setup can be found in the study of Welch *et al.* (*38*).

An orthogonal compositional gradient was achieved by cosputtering from two sputter guns on opposing sides of the substrate in a concentric setup with a deposition angle of roughly 20° and a target-to-substrate distance of 10 cm. The two sputter guns were equipped with ceramic SnS and CaS targets (99.9% purity). Pure argon (99.99% purity) was used as process gas. The process pressure was kept at 2.0×10^{-3} mbar for the duration of the deposition, as well as for the subsequent cooling step. To cover a wide variety of compositional spreads, the sputter powers were adjusted for different libraries resulting in different flux ratios. The power for the CaS sputter gun (P_{CaS}) was kept constant at 40 W, whereas the power for the SnS sputter gun (P_{SnS}) varied from 15 W to 20 W. Depending on the position in the substrate, sputter rates between 2.5 and 1 nm/min were achieved. Deposition times in excess of 8 hours were chosen to produce films with thicknesses ranging from 500 nm for the Ca-rich regions of the films to 1500 nm for the Ca-poor regions of the films.

The $Mn_{1-x}Zn_xO$ samples were deposited using PLD following the deposition method as described by Peng *et al.* (*3*). Specifically, for the TEM analysis, $Mn_{1-x}Zn_xO$ single-temperature, single-composition samples were deposited on EXG borosilicate glass using substrate temperatures of 300° and 550°C, respectively. The films' thicknesses, evaluated by spectroscopic ellipsometry (Woollam M-2000), ranged from 125 to 136 nm. All $Mn_{1-x}Zn_xO$ films were grown in a UHV deposition chamber and deposited by simultaneous ablation of MnO and ZnO targets using a KrF (λ = 248 nm; τ_{FWHM} = 25 ns) laser source (Coherent). Before the depositions, the chamber was filled with flowing O_2 (at a pressure of $pO_2 = 10^{-5}$ torr) and Ar to reach the total pressure (pO_2 + pAr) of 5 mtorr. Laser fluence was set at 4 J/cm^2, and frequency repetition rate was 40 Hz. All coatings were grown at a target-substrate separation distance of 7 cm.

Spatially resolved XRD

The $Sn_{1-x}Ca_xS$ libraries and the $Mn_{1-x}Zn_xO$ samples were investigated in regard to structural and optoelectronic properties using spatially resolved XRD, XRF, UV-Vis, and four-point probe measurements. The XRD measurements were carried out in a Bruker D8 Discover x-ray diffractometer in 2θ geometry using Cu Kα radiation. The composition and thickness were mapped using XRF (Fischerscope XDV-SDD). UV-Vis transmission and reflection measurements were taken in a custom setup covering a wavelength range from 300 to 1100 nm. All combinatorial data sets were evaluated with Igor Pro software using customized routines.

For a determination of the single-phase boundaries in the $Sn_{1-x}Ca_xS$ samples, using XRD data, the disappearing phase method was used (*24*). The area under the curve for the RS-(131) reflex was calculated for different compositions and deposition temperatures. The compositional value *x* for the single-phase boundaries between the nonequilibrium metastable single-phase and two-phase region was then determined by an extrapolation of the areal intensity to zero for each temperature.

Transmission electron microscopy

TEM was performed on samples prepared site-specifically from the $Sn_{1-x}Ca_xS$ and $Mn_{1-x}Zn_xO$ combinatorial libraries using standard focused ion beam thinning and in situ lift-out techniques. Specific regions of interest corresponding to compositions of interest were identified using an FEI Co. Nova 200 dual-column instrument operating at electron energies of 5 keV. An electron beam–induced Pt deposition of ~50 nm thickness was used to protect the sample surface followed by a thicker Pt deposition using a Ga ion accelerating voltage of 30 kV. The same Ga ion energies were used to perform rough milling and in situ extraction to a Cu grid. The final thinning was completed at Ga ion accelerating voltages of 5 kV before examination in an FEI Co. Talos F200X (S)TEM operating at 200 keV. Energy-dispersive spectroscopy was performed using a nominally 1.5-nA STEM probe at count rates of up to 125 kilocounts per second using four windowless detectors to obtain the spectral images (1000 × 1000 pixels), which were then analyzed using the Esprit version 1.9 software package (Bruker

Inc.). Quantification of the compositional profiles extracted from the 2D spectral images was completed using Cliff-Lorimer correction factors and by fixed referencing of the anion concentration to 50 atomic %.

REFERENCES AND NOTES

1. J. C. Hemminger, J. Sarrao, G. Crabtree, G. Flemming, M. Ratner, *Challenges at the Frontiers of Matter and Energy: Transformative Opportunities for Discovery Science* (U.S. Department of Energy Office of Science, 2015).
2. T. F. Kuech, S. E. Babcock, L. Mawst. Growth far from equilibrium: Examples from III-V semiconductors. *Appl. Phys. Rev.* **3**, 040801 (2016).
3. H. Peng, P. F. Ndione, D. S. Ginley, A. Zakutayev, S. Lany, Design of semiconducting tetrahedral $Mn_{1-x}Zn_xO$ alloys and their application to solar water splitting. *Phys. Rev. X* **5**, 021016 (2015).
4. J. Vidal, S. Lany, J. Francis, R. Kokenyesi, J. Tate, Structural and electronic modification of photovoltaic SnS by alloying. *J. Appl. Phys.* **115**, 113507 (2014).
5. Y. Saito, H. Takao, T. Tani, T. Nonoyama, K. Takatori, T. Homma, T. Nagaya, M. Nakamura, Lead-free piezoceramics. *Nature* **432**, 84–87 (2004).
6. J. Greeley, M. Mavrikakis, Alloy catalysts designed from first principles. *Nat. Mater.* **3**, 810–815 (2004).
7. S. F. Chichibu, A. Uedono, T. Onuma, B. A. Haskell, A. Chakraborty, T. Koyama, P. T. Fini, S. Keller, S. P. DenBaars, J. S. Speck, U. K. Mishra, S. Nakamura, S. Yamaguchi, S. Kamiyama, H. Amano, I. Akasaki, J. Han, T. Sota, Origin of defect-insensitive emission probability in In-containing (Al,In,Ga)N alloy semiconductors. *Nat. Mater.* **5**, 810–816 (2006).
8. A. Schleife, M. Eisenacher, C. Rödl, F. Fuchs, J. Furthmüller, F. Bechstedt, Ab initio description of heterostructural alloys: Thermodynamic and structural properties of $Mg_xZn_{1-x}O$ and $Cd_xZn_{1-x}O$. *Phys. Rev. B* **81**, 245210 (2010).
9. F. Tasnádi, B. Alling, C. Höglund, G. Wingqvist, J. Birch, L. Hultman, I. A. Abrikosov, Origin of the anomalous piezoelectric response in wurtzite $Sc_xAl_{1-x}N$ alloys. *Phys. Rev. Lett.* **104**, 137601 (2010).
10. M. Ahart, M. Somayazulu, R. E. Cohen, P. Ganesh, P. Dera, H.-k. Mao, R. J. Hemley, Y. Ren, P. Liermann, Z. Wu, Origin of morphotropic phase boundaries in ferroelectrics. *Nature* **451**, 545–548 (2008).
11. T. Chookajorn, H. A. Murdoch, C. A. Schuh, Design of stable nanocrystalline alloys. *Science* **337**, 951–954 (2012).
12. E. Perim, D. Lee, Y. Liu, C. Toher, P. Gong, Y. Li, W. N. Simmons, O. Levy, J. J. Vlassak, J. Schroers, S. Curtarolo, Spectral descriptors for bulk metallic glasses based on the thermodynamics of competing crystalline phases. *Nat. Commun.* **7** 12315 (2016).
13. M. Beck-Broichsitter, E. Rytting, T. Lebhardt, X. Wang, T. Kissel, Preparation of nanoparticles by solvent displacement for drug delivery: A shift in the "ouzo region" upon drug loading. *Eur. J. Pharm. Sci.* **41**, 244–253 (2010).
14. S. A. Vitale, J. L. Katz, Liquid droplet dispersions formed by homogeneous liquid-liquid nucleation: "The ouzo effect". *Langmuir* **19**, 4105–4110 (2003).
15. F. S. Bates, Polymer-polymer phase behavior. *Science* **251**, 898–905 (1991).
16. N. Horiuchi, Light-emitting diodes: Natural white light. *Nat. Photonics* **4**, 738 (2010).
17. S. T. Tan, X. W. Sun, H. V. Demir, S. P. DenBaars, Advances in the LED materials and architectures for energy-saving solid-state lighting toward "lighting revolution". *IEEE Photon. J.* **4**, 613–619 (2012).
18. S. Strite, H. Morkoç, GaN, AlN, and InN: A review. *J. Vac. Sci. Technol. B* **10**, 1237–1266 (1992).
19. I.-h. Ho, G. B. Stringfellow, Solid phase immiscibility in GaInN. *Appl. Phys. Lett.* **69**, 2701–2703 (1996).
20. G. B. Stringfellow, *Organometallic Vapor-Phase Epitaxy: Theory and Practice* (Academic Press, 1999).
21. L. K. Teles, J. Furthmüller, L. M. R. Scolfaro, J. R. Leite, F. Bechstedt, First-principles calculations of the thermodynamic and structural properties of strained $In_xGa_{1-x}N$ and $Al_xGa_{1-x}N$ alloys. *Phys. Rev. B* **62**, 2475–2485 (2000).
22. R. Smoluchowski, *Phase Transformations in Solids* (Wiley, 1951).
23. E. R. Segnit, A. E. Holland, The system MgO-ZnO-SiO_2. *J. Am. Chem. Soc.* **48**, 409–413 (1965).
24. B. D. Cullity, *Elements of X-ray Diffraction* (Addison-Wesley, 1959).
25. S. Roy, S. Goedecker, V. Hellmann, Bell-Evans-Polanyi principle for molecular dynamics trajectories and its implications for global optimization. *Phys. Rev. E* **77**, 056707 (2008).
26. F. Jensen, *Computational Chemistry* (Wiley, 1999).
27. P. Sinsermsuksakul, J. Heo, W. Noh, A. S. Hock, R. G. Gordon, Atomic layer deposition of tin monosulfide thin films. *Adv. Energy Mater.* **1**, 1116–1125 (2011).
28. B. R. Ortiz, H. Peng, A. Lopez, P. A. Parilla, S. Lany, E. S. Toberer, Effect of extended strain fields on point defect phonon scattering in thermoelectric materials. *Phys. Chem. Chem. Phys.* **17**, 19410–19423 (2015).
29. G. Kresse, J. Furthmüller, Efficient iterative schemes for *ab initio* total-energy calculations using a plane-wave basis set. *Phys. Rev. B* **54**, 11169–11186 (1996).
30. G. Kresse, D. Joubert, From ultrasoft pseudopotentials to the projector augmented-wave method. *Phys. Rev. B* **59**, 1758–1775 (1999).
31. J. P. Perdew, K. Burke, M. Ernzerhof, Generalized gradient approximation made simple. *Phys. Rev. Lett.* **77**, 3865–3868 (1996).
32. H. Peng, S. Lany, Polymorphic energy ordering of MgO, ZnO, GaN, and MnO within the random phase approximation. *Phys. Rev. B* **87**, 174113 (2013).
33. J. Harl, G. Kresse, Cohesive energy curves for noble gas solids calculated by adiabatic connection fluctuation-dissipation theory. *Phys. Rev. B* **77**, 045136 (2008).
34. S. Lany, H. Raebiger, A. Zunger, Magnetic interactions of Cr-Cr and Co-Co impurity pairs in ZnO within a band-gap corrected density functional approach. *Phys. Rev. B* **77**, 241201 (2008).
35. M. L. Green, I. Takeuchi, J. R. Hattrick-Simpers, Applications of high throughput (combinatorial) methodologies to electronic, magnetic, optical, and energy-related materials. *J. Appl. Phys.* **113**, 231101 (2013).
36. A. Zakutayev, J. D. Perkins, P. A. Parilla, N. E. Widjonarko, A. K. Sigdel, J. J. Berry, D. S. Ginley, Zn–Ni–Co–O wide-band-gap p-type conductive oxides with high work functions. *MRS Commun.* **1**, 23–26 (2011).
37. A. Subramaniyan, J. D. Perkins, R. P. O'Hayre, S. Lany, V. Stevanovic, D. S. Ginley, A. Zakutayev, Non-equilibrium deposition of phase pure Cu_2O thin films at reduced growth temperature. *APL Mater.* **2**, 022105 (2014).
38. A. W. Welch, P. Zawadzki, S. Lany, C. A. Wolden, A. Zakutayev, Self-regulated growth and tunable properties of $CuSbS_2$ solar absorbers. *Sol. Energ. Mater. Sol. Cells* **132**, 499–506 (2015).

Acknowledgments

Funding: This work was supported by the U.S. Department of Energy, Office of Science, Office of Basic Energy Sciences, as part of the Energy Frontier Research Center "Center for Next Generation of Materials by Design" under contract no. DE-AC36-08GO28308 to the National Renewable Energy Laboratory (NREL). High Performance Computing resources were sponsored by the U.S. Department of Energy's Office of Energy Efficiency and Renewable Energy, located at NREL. **Author contributions:** S.L. and A.M.H. conceived the project and wrote the manuscript with contributions from S.S., A.Z., and M.F.T. A.M.H. and H.P. performed the computational work, supervised by S.L. S.S. and A.Z. performed the combinatorial thin-film synthesis and characterization of (Sn,Ca)S alloys with assistance from J.D.P. on the extended x-ray measurements. B.E.M. and J.T. performed in parallel synthesis and characterization of (Sn,Ca)S samples by PLD, on which L.T.S. performed x-ray studies (to be reported elsewhere). P.F.N. synthesized the (Mn,Zn)O samples for the TEM characterization. B.P.G. performed the focused ion beam and TEM analysis. All authors contributed to discussions advancing the project and commented on the manuscript. **Competing interests:** The authors declare that they have no competing interests. **Data and materials availability:** All data needed to evaluate and reproduce the conclusions in this article are present within and/or available online for free at https://materials.nrel.gov. Additional data related to this article may be requested from the authors.

Submitted 25 January 2017
Accepted 12 April 2017
Published 7 June 2017
10.1126/sciadv.1700270

Citation: A. M. Holder, S. Siol, P. F. Ndione, H. Peng, A. M. Deml, B. E. Matthews, L. T. Schelhas, M. F. Toney, R. G. Gordon, W. Tumas, J. D. Perkins, D. S. Ginley, B. P. Gorman, J. Tate, A. Zakutayev, S. Lany, Novel phase diagram behavior and materials design in heterostructural semiconductor alloys. *Sci. Adv.* **3**, e1700270 (2017).

Novel phase diagram behavior and materials design in heterostructural semiconductor alloys

Aaron M. Holder, Sebastian Siol, Paul F. Ndione, Haowei Peng, Ann M. Deml, Bethany E. Matthews, Laura T. Schelhas, Michael F. Toney, Roy G. Gordon, William Tumas, John D. Perkins, David S. Ginley, Brian P. Gorman, Janet Tate, Andriy Zakutayev and Stephan Lany (June 7, 2017)

Sci Adv 2017, 3:.
doi: 10.1126/sciadv.1700270